On the investigation of shock wave/boundary layer interaction with a high-order scheme based on lattice Boltzmann flux solver

Jian Qin[1,2], Haichuan Yu[3] and Jie Wu[1,2]*

*Correspondence:
wuj@nuaa.edu.cn

[1] State Key Laboratory
of Mechanics and Control
of Mechanical Structures,
Nanjing University
of Aeronautics and Astronautics,
Nanjing 210016, China
[2] Key Laboratory of Unsteady
Aerodynamics and Flow
Control, Ministry of Industry
and Information Technology,
Department of Aerodynamics,
Nanjing University
of Aeronautics and Astronautics,
Nanjing 210016, China
[3] China Academy of Launch
Vehicle Technology,
Beijing 100076, China

Abstract

Shock wave/boundary layer interaction (SWBLI) continues to pose a significant challenge in the field of aerospace engineering. This paper aims to address this issue by proposing a novel approach for predicting aerodynamic coefficients and heat transfer in viscous supersonic and hypersonic flows using a high-order flux reconstruction technique. Currently, finite volume methods are extensively employed for the computation of skin aerodynamic coefficients and heat transfer. Nevertheless, these numerical methods exhibit considerable susceptibility to a range of factors, including the inviscid flux function and the computational mesh. The application of high-order flux reconstruction techniques offers promising potential in alleviating these challenges. In contrast to other high-order methods, the flux reconstruction is combined with the lattice Boltzmann flux solver in this study. The current method evaluates the common inviscid flux at the cell interface by locally reconstructing the lattice Boltzmann equation solution from macroscopic flow variables at solution points. Consequently, this framework performs a positivity-preserving, entropy-based adaptive filtering method for shock capturing. The present approach is validated by simulating the double Mach reflection, and then simulating some typical viscous problems. The results demonstrate that the current method accurately predicts aerodynamic coefficients and heat transfer, providing valuable insights into the application of high-order methods for shock wave/boundary layer interaction.

Keywords: Shock wave/boundary layer interaction, High order method, Flux reconstruction, Lattice Boltzmann flux solver, Entropy-based adaptive filtering method

1 Introduction

In the study of supersonic and hypersonic problems, shock wave/boundary layer interaction is one of the most common complex flow phenomena. These complex phenomena can significantly affect the aerodynamics and thermodynamics of aerospace vehicles. An accurate understanding of their dynamics can contribute greatly to the development of the aerospace vehicles. In particular, flows around transonic airfoils, supersonic intakes and supersonic suction engines can lead to flow separation, increase in drag force, and performance loss due to these interactions. After the shock wave incident at the boundary, it continues to exist within the boundary layer and blocks the pressure difference

between the front and back of the wave. However, the inverse pressure gradient across the shock wave can be transmitted from downstream to upstream of the shock wave through the subsonic zone of the boundary layer, resulting in flow separation and the formation of a separated shock wave upstream. Furthermore, SWBLI generally produces unstable shock wave systems at low frequencies, which can alter or induce fatigue damage to thermally loaded structures. The problems caused by these issues make SWBLI one of the most challenging issues in the research of hypersonic vehicles.

In view of the aforementioned problems, it is known that SWBLI could be effectively studied using canonical configurations such as compression corners, shock impingement cases, double cones, double wedges, single and double fins. Supersonic and hypersonic flows over ramps have been experimentally investigated for their effect on angle of ramp, wall temperature, and plate length [1–3]. An experimental study conducted by Elena and Lacharme [4] measured the velocity, Reynolds tangential stresses, skewness and flatness factors, and intermittency factor at a free-stream Mach number of 2.3. The results obtained indicate that the boundary measurements are in good agreement with previous data. Some research done by Settles et al. [5–7] utilized wind tunnel experiments with Mach number 2.85 compression ramp to provide experimental measurements of boundary layer thickness, velocity profiles, surface pressures, and skin friction coefficients. Bookey et al. [8] performed an experimental study of supersonic 24° and 8° compression ramp conducted with the free stream Mach numbers 2.9 and 8, respectively. Marini [9] investigated the SWBLI phenomena over a two-dimensional ramp in a wind tunnel, verifying or establishing separation characteristics, dynamic and thermal loads, and aerodynamic performance. Experiments of turbulent and laminar SWBLI from supersonic and hypersonic flows over the ramp were conducted by Hankey and Holden [10], who studied the effect of Reynolds number, ramp angle, and Mach number on upstream influence. The effect of bluntness on pressure and thermal loads was also considered.

Numerical simulation techniques have been proven to be an effective means of studying SWBLI, in addition to the experiments. Rizzetta and Mach [11] simulated hypersonic compression corner flows using four different numerical algorithms. John et al. [12, 13] simulated the two-dimensional ramp induced flow to investigate the effect of various geometrical and flow parameters on the laminar boundary layer separation. The details of upstream influence, length of separation bubble, separation point pressure, and heat transfer were examined. Brioso et al. [14] indicated that increasing the wall temperature leads to the separation and reattachment points moving upstream and downstream, respectively. Kane and Peetala [15] studied the detailed physics of laminar boundary layer separation in hypersonic ramp flow using OpenFOAM, an open source software. Kotteda and Mittal [16] developed a stabilized finite element method for the numerical solution of SWBLI with Mach number up to 3. Employing the high-order hybridizable discontinuous Galerkin method, Moro et al. [17] performed some simulations of SWBLI, such as supersonic flow in a duct with a ramp, supersonic flow inside a scramjet combustor, and supersonic flow over a forward facing step. Adams [18, 19] was the first to perform the direct numerical simulation (DNS) of supersonic compression ramp. Wu and Martin [20] performed DNS for a 24° compression ramp configuration following the experiment of Bookey et al. [8]. Loginov

et al. [21] performed the large-eddy simulation of a $25°$ compression ramp at Mach number 2.95, resulting in good agreement with experimental data.

Numerical simulations have been proven promising in predicting the dynamics of SWBLI for over 70 years. However, accuracy issues have been a major constraint on their development. As Katzer [22] introduced dissipation in the simulations of oblique SWBLI, which adversely affected the height of the separating vortex, the development of high-resolution, low-dissipation numerical formats is particularly important in the numerical simulation of shock interference problems. Most studies analyzed SWBLI under the second order accuracy, and some studies were simulated in a high-order framework but with low Mach numbers. In recent years, higher order formats have received increasing attention. Compared with traditional formats, high-order formats can achieve higher accuracy with fewer grids, and have lower dissipation and higher resolution. This range of higher order formats includes essentially non-oscillatory scheme [23], weighted essentially non-oscillatory scheme [24], discontinuous Galerkin (DG) method [25], spectral difference (SD) [26], and so on. The flux reconstruction (FR) approach proposed by Huynh [27] has been attracting a lot of interest. This approach is able to restore to nodal DG [28] and SD in a unified framework, at least for a linear flux function.

In this work, a high-order FR scheme combined with the lattice Boltzmann flux solver [29], named as FR-LBFS, is employed to simulate SWBLI. Considering real physical effects, the FR-LBFS can achieve positive density and pressure in the case of strong shock waves and discontinuities. The entropy-based adaptive filtering method [30] is utilized to capture the shock wave, which exhibits excellent density and pressure positivity preservation properties without specific free parameters. Different from the finite volume method used in Ref. [29], the current method employs the FR approach, which can get arbitrary high order accuracy by adding solution points, and it is inherently suitable for parallel computing. However, to achieve higher order accuracy in finite volume methods, extensive reconstruction templates are required, and parallel computing and boundary handling become significantly challenging. On the other hand, the original LBFS [29] did not systematically investigate SWBLI issues at high Mach numbers. Meanwhile, in high-order finite element methods, the majority of SWBLI simulations are based on DG methods. Compared to the DG method, the FR method allows larger time steps [31], and some studies have shown that the FR method is more efficient than the DG method [32, 33]. Hence, this paper employs the FR method for simulating SWBLI. In the work of Zhang et al. [34], a third-order accurate gas kinetic scheme based on the Maxwellian distribution function was employed in the correction procedure via the reconstruction framework. Due to the intricate nature of the Maxwellian function, this method tends to be more intricate and less efficient compared to traditional numerical methods [35, 36]. The time discretization is implemented using a third-order three-stage Runge-Kutta method [37]. The rest of the paper is organized in the following way. Section 2 provides the basic formulation of the current method. Numerical simulations of some typical SWBLI problems are given in Section 3. Section 4 presents the conclusions.

2 Methodology

2.1 Governing equations

The governing equation for two-dimensional viscous compressible flows solved in this paper is expressed as follows:

$$\frac{\partial \mathbf{Q}}{\partial t} + \frac{\partial \mathbf{F}}{\partial x} + \frac{\partial \mathbf{G}}{\partial y} = 0, \tag{1}$$

where $\mathbf{Q} = (\rho, \rho u, \rho v, \rho e)$ is the conservative variable vector. ρ is the density, u and v are the components of velocity vector. e is the total energy per unit mass of gas, and it is related to the total specific internal energy E, which is written as

$$E = \rho e = \frac{p}{\gamma - 1} + \frac{1}{2}\rho\left(u^2 + v^2\right), \tag{2}$$

where p denotes the pressure, and γ denotes the specific heat ratio. $\mathbf{F}$ and $\mathbf{G}$ in Eq. (1) are the corresponding x and y directional flux vectors, respectively. Inviscid fluxes and viscous fluxes are involved in them. The inviscid fluxes are

$$\mathbf{F}_{inv} = \begin{bmatrix} \rho u \\ \rho u^2 + p \\ \rho uv \\ u(E + p) \end{bmatrix}, \mathbf{G}_{inv} = \begin{bmatrix} \rho v \\ \rho uv \\ \rho v^2 + p \\ v(E + p) \end{bmatrix}, \tag{3}$$

and the viscous fluxes are

$$\mathbf{F}_{vis} = \begin{bmatrix} 0 \\ \tau_{xx} \\ \tau_{xy} \\ u\tau_{xx} + v\tau_{xy} - q_x \end{bmatrix}, \mathbf{G}_{vis} = \begin{bmatrix} 0 \\ \tau_{yx} \\ \tau_{yy} \\ u\tau_{yx} + v\tau_{yy} - q_y \end{bmatrix}, \tag{4}$$

where τ_{ij} and q_i represent the viscous stress tensor and heat flux, respectively, which are written as

$$\tau_{ij} = \mu\left(\frac{\partial u_i}{\partial x_j} + \frac{\partial u_j}{\partial x_i} - \frac{2}{3}\delta_{ij}\frac{\partial u_k}{\partial x_k}\right), q_i = -\lambda\frac{\partial T}{\partial x_i}, \tag{5}$$

where μ denotes the dynamic viscosity, calculated by Sutherland's law. δ_{ij} is the Kronecker symbol. λ is the thermal conductivity, which is connected with μ through the Prandtl number, $Pr = 0.71$. T is the temperature.

2.2 Flux reconstruction formulation based on LBFS

In this sub-section, we will briefly describe the FR scheme based on the LBFS. The whole computational domain Ω is split into N non-overlapping elements Ω_n. In order to facilitate the calculation, each element is mapped to a standard element $I = [-1, 1] \times [-1, 1]$. The coordinate system of the standard element is represented by (ξ, η), and so the mapping relationship between the global coordinate system (x, y) in the physical domain Ω_n and the local coordinate system (ξ, η) of the standard element Ω_s is presented as follows:

$$\begin{bmatrix} x(\xi, \eta) \\ y(\xi, \eta) \end{bmatrix} = \sum_{i=1}^{K} M_i(\xi, \eta)\begin{pmatrix} x_i \\ y_i \end{pmatrix}, \tag{6}$$

where K is the number of nodes defined in the element, and $M_i(\xi, \eta)$ is a shape function. By using the conversion relation in Eq. (6), Eq. (1) becomes
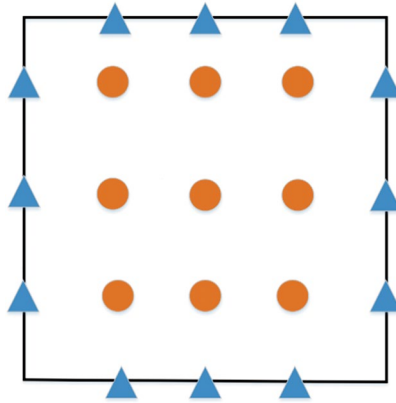
Fig. 1 The distribution of solution points (circle) and flux points (triangle)

$$\frac{\partial \hat{\mathbf{Q}}}{\partial t} + \frac{\partial \hat{\mathbf{F}}}{\partial \xi} + \frac{\partial \hat{\mathbf{G}}}{\partial \eta} = 0, \tag{7}$$

where

$$\hat{\mathbf{Q}} = |\mathbf{J}| \, \mathbf{Q}, \begin{bmatrix} \hat{\mathbf{F}} \\ \hat{\mathbf{G}} \end{bmatrix} = |\mathbf{J}|\mathbf{J}^{-1} \begin{bmatrix} \mathbf{F} \\ \mathbf{G} \end{bmatrix}, \tag{8}$$

where $\mathbf{J}$ is the Jacobian of the mapping function

$$\mathbf{J} = \begin{pmatrix} x_\xi & x_\eta \\ y_\xi & y_\eta \end{pmatrix}, \tag{9}$$

and $|\mathbf{J}|$ is the determinant of the Jacobian matrix.

Inside every element, a polynomial of order P is used to denote $(P+1)$-order accuracy of the solution and the flux. For solution in the two-dimensional element, it is a tensor product of the one-dimensional Gauss-Legendre points. On the other hand, flux points are defined on cell boundaries, as shown in Fig. 1. To be consistent with the location of the solution point, the flux is a tensor product of the one-dimensional Gauss-Legendre points along each edge. The approximate solution and flux polynomials are expressed as follows:

$$\hat{\mathbf{Q}}^D = \sum_{i=1}^{P+1} \sum_{j=1}^{P+1} \hat{\mathbf{Q}}_{i,j}^D \ell_i(\xi)\ell_j(\eta), \hat{\mathbf{F}}^D(\xi,\eta) = \sum_{i=1}^{P+1} \sum_{j=1}^{P+1} \hat{\mathbf{F}}_{i,j}^D \ell_i(\xi)\ell_j(\eta), \tag{10}$$

where $\hat{\mathbf{Q}}_{i,j}^D$ is the transformed solution value at the point (ξ_i, η_j), $\hat{\mathbf{F}}_{i,j}^D$ is the transformed flux value at the point (ξ_i, η_j), and $P+1$ denotes the number of flux points in the

one-dimensional direction. $\ell_i(X)$ denotes the Lagrange interpolation basis, which can be described as

$$\ell_i(X) = \prod_{k=1,i\neq k}^{P+1} \left(\frac{X - X_k}{X_i - X_k} \right), i = 1, 2, 3, \ldots, P+1. \tag{11}$$

At the interface, however, the flux is discontinuous and excludes the effect of the adjacent element. In order to contain the influence of the adjacent element, the common flux $\hat{\mathbf{F}}^{com}$ at the element interface should be taken into account. Define the continuous flux polynomial $\hat{\mathbf{F}}_i^C(\xi)$ of the element i in ξ direction, the correction to the discontinuous flux function is made by

$$\hat{\mathbf{F}}_i^C(\xi) = \hat{\mathbf{F}}_i^D(\xi) + \left(\hat{\mathbf{F}}_L^{com} - \hat{\mathbf{F}}_i(-1) \right) c_L(\xi) + \left(\hat{\mathbf{F}}_R^{com} - \hat{\mathbf{F}}_i(1) \right) c_R(\xi), \tag{12}$$

where $\hat{\mathbf{F}}_L^{com}$ and $\hat{\mathbf{F}}_R^{com}$ are the common fluxes at the left and right boundaries of the element, respectively. c_L and c_R represent correction functions of the left and right boundaries, respectively. c_L and c_R should satisfy the following conditions:

$$c_L(-1) = 1, c_L(1) = 0, c_R(-1) = 0, c_R(1) = 1. \tag{13}$$

For the sake of the proper flux, it is necessary to compute the flux at the interface $\hat{\mathbf{F}}^{com}$ using the approximate Riemann solver. $\hat{\mathbf{F}}^{com}$ contains inviscid flux $\hat{\mathbf{F}}_{inv}^{com}$ and viscous flux $\hat{\mathbf{F}}_{vis}^{com}$, i.e., $\hat{\mathbf{F}}^{com} = \hat{\mathbf{F}}_{inv}^{com} + \hat{\mathbf{F}}_{vis}^{com}$. In this work, the LBFS [29] is applied to compute $\hat{\mathbf{F}}_{inv}^{com}$, and $\hat{\mathbf{F}}_{vis}^{com}$ is computed by the local DG (LDG) [38] method. The principle of the LBFS model within the FR framework can be illustrated in Fig. 2.

In this work, the D1Q4 LBFS model is adopted. Because the LBFS is adopted in the one-dimensional direction, it is necessary to convert the conservation variable $\mathbf{Q}$ and the inviscid flux $\mathbf{F}_{inv}$ in Eq. (1) into the tangential and normal components of velocity, such as follows:
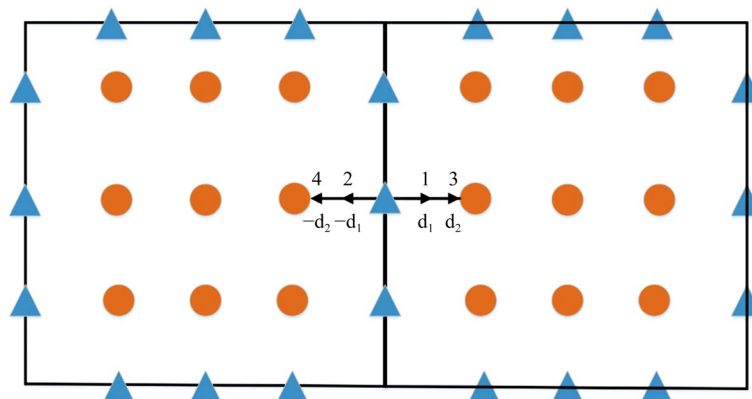
Fig. 2 Local reconstruction of the lattice Boltzmann solution at flux points

$$\mathbf{Q} = \begin{bmatrix} \rho \\ \rho(u_n\mathbf{n} + \mathbf{u}_t) \\ \rho\left(\frac{u_n^2}{2} + e\right) + \frac{\rho|\mathbf{u}_t|^2}{2} \end{bmatrix}, \tag{14}$$

$$\mathbf{F}_{inv} = \begin{bmatrix} \rho u_n \\ \left(\rho u_n^2 + p\right)\mathbf{n} + \rho u_n\mathbf{u}_t \\ \left(\rho\left(\frac{u_n^2}{2} + e\right) + p\right)u_n + \frac{\rho u_n|\mathbf{u}_t|^2}{2} \end{bmatrix}, \tag{15}$$

where u_n denotes the normal velocity of the cell interface; correspondingly, $\mathbf{u}_t$ is the tangential velocity of the cell interface. Based on the moment relationship equation [29], the conservative variable and inviscid flux depending on the normal velocity can be calculated by the distribution function $f_i(\mathbf{r},t)$ as follows:

$$\overline{\mathbf{Q}} = \begin{bmatrix} \rho & \rho u_n & \rho\left(\frac{u_n^2}{2} + e\right) \end{bmatrix}^T = \sum_{i=1}^{4} \varphi_\alpha f_i(\mathbf{r}, t), \tag{16}$$

$$\overline{\mathbf{F}}_{inv} = \begin{bmatrix} \rho u_n & \rho u_n^2 + p & \left(\rho\left(\frac{u_n^2}{2} + e\right) + p\right)u_n \end{bmatrix}^T = \sum_{i=1}^{4} \varsigma_i \varphi_\alpha f_i(\mathbf{r}, t), \tag{17}$$

where ς_i is the velocity of the particle in the i-th direction. In the current D1Q4 LBFS model, $\varsigma_1 = d_1, \varsigma_2 = -d_1, \varsigma_3 = d_2, \varsigma_4 = -d_2$, where d_1 and d_2 are particle speeds [29]. φ_α is the moment. $f_i(\mathbf{r},t)$, φ_α, d_1 and d_2 are defined as

$$f_1^{eq} = \frac{\rho\left(-d_1 d_2^2 - d_2^2 u + d_1 u^2 + d_1 c^2 + u^3 + 3uc^2\right)}{2d_1\left(d_1^2 - d_2^2\right)},$$

$$f_2^{eq} = \frac{\rho\left(-d_1 d_2^2 + d_2^2 u + d_1 u^2 + d_1 c^2 - u^3 - 3uc^2\right)}{2d_1\left(d_1^2 - d_2^2\right)},$$

$$f_3^{eq} = \frac{\rho\left(d_1^2 d_2 + d_1^2 u - d_2 u^2 - d_2 c^2 - u^3 - 3uc^2\right)}{2d_2\left(d_1^2 - d_2^2\right)},$$

$$f_4^{eq} = \frac{\rho\left(d_1^2 d_2 - d_1^2 u - d_2 u^2 - d_2 c^2 + u^3 + 3uc^2\right)}{2d_2\left(d_1^2 - d_2^2\right)},$$

$$d_1 = \sqrt{u^2 + 3c^2 - \sqrt{4u^2c^2 + 6c^4}},$$

$$d_2 = \sqrt{u^2 + 3c^2 + \sqrt{4u^2c^2 + 6c^4}},$$

$$\varphi_\alpha = \begin{bmatrix} 1 & \varsigma_i & \frac{\varsigma_i^2}{2} + e_p \end{bmatrix}^T. \tag{18}$$

In the above expression, e_p is the particle velocity potential energy, which is in the following form of $e_p = \left[1 - \frac{1}{2}(\gamma - 1)\right]e_m$, where e_m is the potential energy of the mean flow, which is defined as $\frac{p}{(\gamma-1)\rho}$.

Substituting the interface distribution function $f_i(\mathbf{r},0)$ into Eqs. (14) and (15), according to Ref. [29], the conservative variable and the inviscid flux at the interface can be calculated via the equilibrium distribution function g_i as follows:

$$
\begin{aligned}
\overline{\mathbf{Q}}^{com} &= \sum_{i=1}^{4} \boldsymbol{\varphi}_\alpha g_i(0,t) \\
\overline{\mathbf{F}}_{inv}^{com} &= \overline{\mathbf{F}}_{inv}^{com,\mathrm{I}} + \tau_0 \left(\overline{\mathbf{F}}_{inv}^{com,\mathrm{II}} - \overline{\mathbf{F}}_{inv}^{com,\mathrm{I}} \right) \\
\overline{\mathbf{F}}_{inv}^{com,\mathrm{I}} &= \sum_{i=1}^{4} \varsigma_i \boldsymbol{\varphi}_\alpha g_i(0,t), \quad \overline{\mathbf{F}}_{inv}^{com,\mathrm{II}} = \sum_{i=1}^{4} \varsigma_i \boldsymbol{\varphi}_\alpha g_i(-\varsigma_i \delta t, t - \delta t)
\end{aligned}
, \tag{19}
$$

where τ_0 can be regarded as a function that controls the numerical dissipation. This means that in the smooth region, τ_0 is chosen to be 0. However, around the discontinuity, τ_0 is set to a non-zero value. The expression for τ_0 is

$$
\tau_0 = \tanh\left(C \frac{|p^L - p^R|}{p^L + p^R} \right), \tag{20}
$$

where p^L and p^R denote left and right pressures at the cell interface, respectively. In this work, C is recommended to be $C = 10$.

It is clear that the solutions of $g_i(0,t)$ and $g_i(-\varsigma_i\delta t, t - \delta t)$ are needed in Eq. (17). Drawing on the idea of the Riemann problem at the cell interface, one can obtain $g_i(-\varsigma_i\delta t, t - \delta t)$. Meanwhile, $g_i(0,t)$ can be calculated by conservative variable at the cell interface. After that, the inviscid flux components at the cell interface $\mathbf{F}_{inv}^{com,\mathrm{I}}$ and $\mathbf{F}_{inv}^{com,\mathrm{II}}$ with respect to the normal and tangential velocities can be calculated, which are expressed as follows:

$$
\mathbf{F}_{inv}^{com,\mathrm{I}} = \overline{\mathbf{F}}_{inv}^{com,\mathrm{I}} + \begin{bmatrix} 0 \\ \rho\mathbf{u}_t u_n \\ \frac{\rho u_n |\mathbf{u}_t|^2}{2} \end{bmatrix}, \tag{21}
$$

$$
\mathbf{F}_{inv}^{com,\mathrm{II}} = \overline{\mathbf{F}}_{inv}^{com,\mathrm{II}} + \begin{bmatrix} 0 \\ \rho\mathbf{u}_t u_n \\ \frac{\rho u_n |\mathbf{u}_t|^2}{2} \end{bmatrix}, \tag{22}
$$

where the components depending on the tangential velocity can be calculated as follows:

$$
\rho\mathbf{u}_t u_n = \sum_{i=1,3} \varsigma_i g_i^L \mathbf{u}_t^L + \sum_{i=2,4} \varsigma_i g_i^R \mathbf{u}_t^R, \tag{23}
$$

$$
\rho u_n |\mathbf{u}_t|^2 = \sum_{i=1,3} \varsigma_i g_i^L \left| \mathbf{u}_t^L \right|^2 + \sum_{i=2,4} \varsigma_i g_i^R \left| \mathbf{u}_t^R \right|^2, \tag{24}
$$

where g_i^L and g_i^R are the left and right equilibrium distribution functions at the cell interface, respectively, which are respectively computed based on the conservative variables on the left and right sides of the interface after the reconstruction. $\mathbf{u}_t^L$ and $\mathbf{u}_t^R$ are the left and right tangential velocities at the cell interface, respectively. Finally, the inviscid flux vector at the interface is calculated as follows:

$$\mathbf{F}_{inv}^{com} = \mathbf{F}_{inv}^{com,\mathrm{I}} + \tau_0 \left(\mathbf{F}_{inv}^{com,\mathrm{II}} - \mathbf{F}_{inv}^{com,\mathrm{I}} \right). \tag{25}$$

Then, converting $\mathbf{F}_{inv}^{com}$ into $\hat{\mathbf{F}}_{inv}^{com}$ in the standard element and using $\hat{\mathbf{F}}_{vis}^{com}$, the flux at the interface $\hat{\mathbf{F}}^{com}$ can be obtained.

The last step is to calculate divergence of the continuous flux for updating the solution.

$$\frac{d\left(\hat{\mathbf{F}}_i^C(\xi) \right)}{d\xi} = \frac{d\left(\hat{\mathbf{F}}_i^D(\xi) \right)}{d\xi} + \left(\hat{\mathbf{F}}_L^{com} - \hat{\mathbf{F}}_i(-1) \right) \frac{d(c_L(\xi))}{d\xi} + \left(\hat{\mathbf{F}}_R^{com} - \hat{\mathbf{F}}_i(1) \right) \frac{d(c_R(\xi))}{d\xi}. \tag{26}$$

The calculation of flux derivative in the η direction can be solved in the same manner. Then we can get the semi-discretized form of the governing system Eq. (7). Finally, this semi-discretized form is a system of ordinary differential equations and can be solved using the Runge-Kutta method [37].

3 Numerical investigation

In this section, the performance of aerodynamics and heat transfer in viscous supersonic and hypersonic flows is studied by FR-LBFS within the PyFR framework [39]. This includes simulating the double Mach reflection, viscous shock tube problem, shock wave/boundary layer interaction, supersonic compressible ramp flow, and hypersonic flow over a leading edge ramp. The time step is around 1e-5 in the following numerical simulations. The pressure coefficient, skin friction coefficient, and Stanton number are defined as follows:

$$C_p = \frac{p - p_\infty}{(1/2)\rho U_\infty^2}, C_f = \frac{\tau_x}{(1/2)\rho U_\infty^2}, St = \frac{q_w}{(1/2)\rho U_\infty C_p (T_r - T_w)},$$

where p_∞ and U_∞ represent the free-stream pressure and velocity, respectively. τ_x and q_w are the viscous stress tensor and heat flux. $T_r = T_\infty \left(1 + r \frac{\gamma-1}{2} Ma^2 \right)$ is the recovery temperature and $r = \sqrt{Pr}$ is the recovery factor.

3.1 Accuracy test

To validate the accuracy of the proposed FR-LBFS method, a manufactured solution case [40], typically employed for accuracy testing in the context of the compressible Navier-Stokes (N-S) equations, is simulated. This manufactured solution serves as the exact solution for the compressible N-S equation.

$$\rho^m = p^m = e^{-5\left[4(x-1/2)^2 + (y-1/2)^2 \right]} + 1. \tag{27}$$
$$u^m = v^m = 1$$

A periodic boundary condition is enforced on all four boundaries within the computational domain $[0, 1] \times [0, 1]$. The simulation adopts a Mach number of 0.4 and a Reynolds number of 1000. Four distinct uniform grids with mesh sizes of $h = 1/10, 1/16, 1/32,$ and $1/64$ are employed. The numerical error of density ρ is quantified using the L_2 norm, which is expressed as follows:

$$L_2 = \sqrt{\sum_{i=1}^{N} \int_{\Omega_i} [\rho(t) - \rho^m(t)]^2 d\Omega_i} \approx \sqrt{\sum_{i=1}^{N} \sum_{j=1}^{N_q} [\rho(t) - \rho^m(t)]^2 J_i \omega_i}, \tag{28}$$

where ρ is the numerical solution, Ω_i denotes the i-th standard element, J_i is the Jacobian determinant corresponding to the i-th element, N and N_q represent the numbers of elements and quadrature points, respectively, and ω_j is the j- quadrature weight.

A convergence study is conducted to demonstrate the accuracy of the proposed FR-LBFS method. The order of accuracy is determined by the slope of the linear least-squares fit of $\log(h) \propto \log(L_2)$. Table 1 presents the errors and convergence orders for the density. The table indicates that the desired order of accuracy can be achieved.

3.2 Double Mach reflection

The double Mach reflection problem has garnered extensive attention due to its relevance to various high-speed applications, including supersonic and hypersonic flight. This problem involves the interaction of supersonic flow with solid obstacles, leading to the generation of strong shock waves reflecting from the obstacle surface. The domain size is $[0, 4] \times [0, 1]$, utilizing a grid resolution of 2400×600 under P2, P3 and P4 conditions. Initially, a right-traveling strong shock with $Ma = 10$ reflects at an angle of $60°$ from the wall. The left boundary and the lower boundary at $x < 1/6$ are set as post-shock conditions. The lower boundary at $x \geq 1/6$ is set as a no-slip adiabatic wall. At the right boundary of the computational domain, a pre-shock condition is applied, and at the upper boundary, a shock condition with $Ma = 10$ is specified. The density ahead of the shock is set to 1.4, the velocity is 0, and the pressure is 1, while the post-shock conditions can be determined based on the shock relations.

Figure 3 presents the density contours along the three Mach stems, showing the intricate flow features and comparing the results at different accuracies. It is evident that the resolution of the P2 results is notably lower than that of P3 and P4. Moreover, the proximity of the P3 and P4 results suggests that the P3 accuracy achieved by this algorithm is satisfactory. Figure 4 displays a close-up view of the flow field near the Mach stems under P3 accuracy, revealing fine vortex structures beneath the three Mach stems.

Table 1 L_2 norm error and order of accuracy for the manufactured solution case

P	Mesh size h	L_2 error	Order
2	1/10	3.40e-4	–
	1/16	8.08e-5	3.05
	1/32	1.02e-5	2.98
	1/64	1.34e-6	2.92
3	1/10	2.32e-5	–
	1/16	3.51e-6	4.02
	1/32	2.18e-7	4.09
	1/64	1.61e-8	3.75

(a) P2

(b) P3

(c) P4
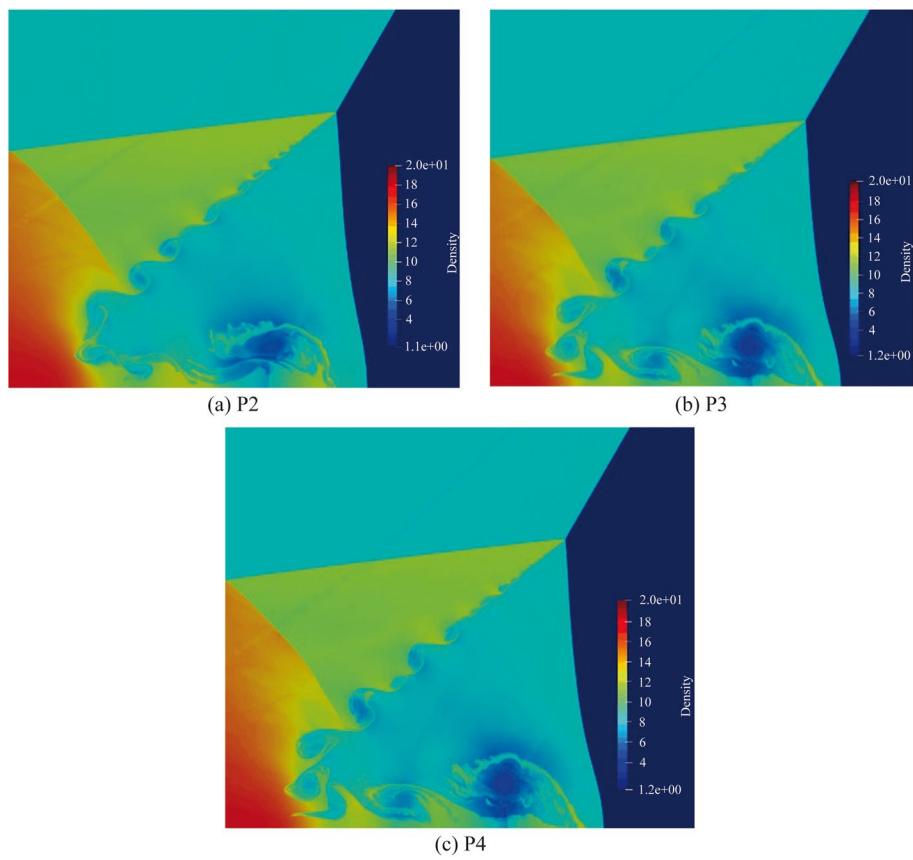
Fig. 3 Contours of the density for double Mach reflection
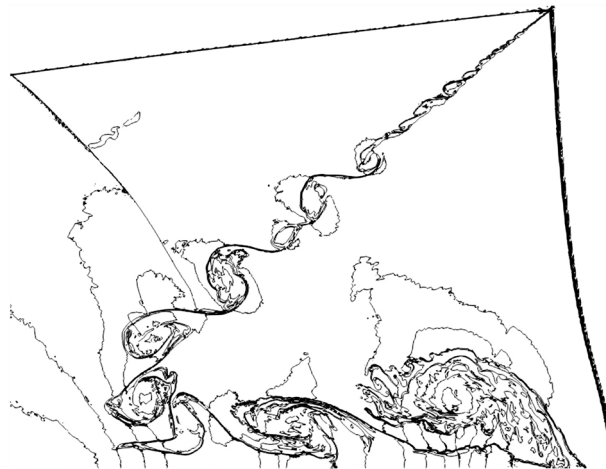
Fig. 4 Local contour lines of the density for double Mach reflection

3.3 Viscous shock tube problem

The viscous shock tube problem, originally proposed by Daru and Tenaud [41], serves as a classical benchmark to evaluate the accuracy and robustness of algorithms in

simulating viscous compressible flows. This challenging scenario involves the intricate interplay between shock waves and boundary layers, necessitating precise numerical schemes. The complexity of this phenomenon arises from the presence of reflected waves, contact discontinuities, shock waves, and their interactions with viscosity. In the computational domain of $[-0.5, 0.5] \times [0, 0.5]$, a uniform grid of 300×150 is employed. The calculations are conducted under the P3 condition. The upper wall is set as a slip boundary condition, while the remaining boundaries are set as a no-slip boundary condition. A thin film separates two different states of gas at $x = 0$ and the initial conditions are presented as follows:

$$(\rho, u, v, p) = \begin{cases} \left(\frac{120, 0, 0, 120}{\gamma} \right), & -0.5 < x < 0 \\ \left(\frac{1.2, 0, 0, 1.2}{\gamma} \right), & 0 < x < 0.5 \end{cases},$$

where $\gamma = 1.4$.

In order to contrast the results under different viscosity, Fig. 5 shows the local density gradient contours for varying viscosity coefficients ($\mu = 0.005$, 0.001, and 0.0001), illustrating the intricate flow structures associated with this complex phenomenon. Notably, these structures encompass λ-shocks and finely detailed vortex patterns.

3.4 Shock wave/boundary layer interaction

The strong shock wave/boundary-layer interaction where a shock impinges on the boundary layer would produce a separation of the flow and a subsequent recirculation bubble. In this case, the shock undergoes a transformation where it no longer reflects off the wall. Instead, it evolves into a combination of an expansion fan at the edge of the boundary layer, along with two compression waves around the separation and reattachment points.

Under the same condition as the work of Degrez et al. [42], the freestream of this case is $Ma = 2.15$ and $Re = 1 \times 10^5$. The computational domain is shown in Fig. 6, which is composed of a flat plate and a shock generator. The left leading edge of the flat plate is designed as a circular arc to avoid the singularity. As seen in Fig. 7, the unstructured grid with 4155 elements is employed. Again, the P3 condition is selected, and it will also be used in the following simulations. The upper side of the domain is an inviscid boundary condition, and the left and right of the domain are supersonic inflow and outflow boundary conditions, respectively. The front of the plate's left leading edge is a symmetry wall and the plate is an adiabatic wall.

(a) $\mu = 0.005$ (b) $\mu = 0.001$
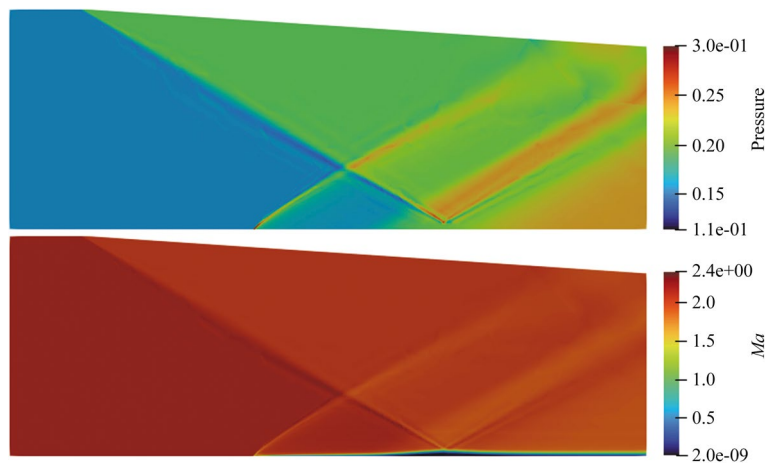
(c) $\mu = 0.0001$
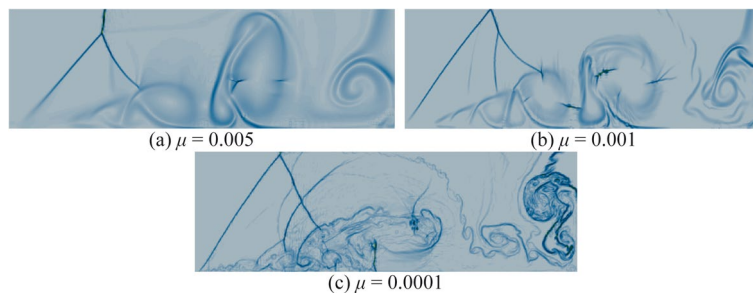
Fig. 5 Contours of the density gradient norm
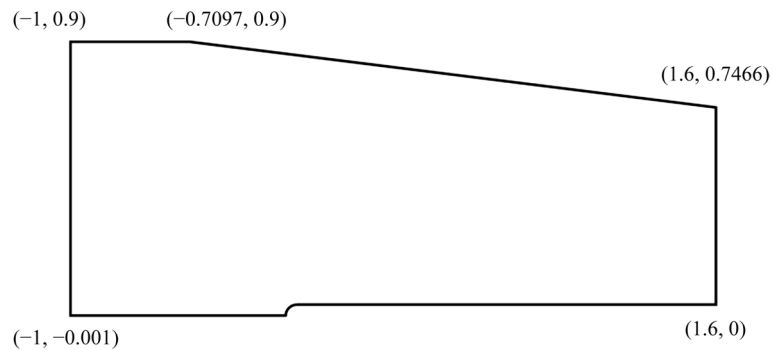
Fig. 6 Computational domain of shock wave/boundary-layer interaction
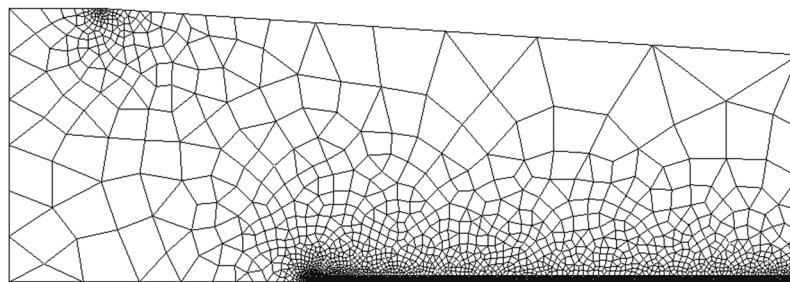
Fig. 7 Grid of shock wave/boundary layer interaction

Fig. 8 Contours of pressure coefficient and Mach number for shock wave/boundary-layer interaction

The contours of pressure coefficient and Mach number are shown in Fig. 8. The presence of shock waves generated at different positions and the influence of strong shock/boundary layer interactions can be observed. This SWBLI demonstrates a good behaviour of the current approach in the resolution of the boundary layer. Simultaneously, it excels in handling the interference between two flow features effectively.

Figure 9 shows the comparison of the pressure coefficient C_p on the plate between the current result and those in literature [42–44]. The present C_p agrees well with the experimental result of Degrez et al. [42] and the numerical result of Moro et al. [43]. It is worth mentioning that the result of Moro et al. [43] is based on highly adaptive meshes, which implies that this method holds a greater advantage compared to other non-adaptive grids. However, the current results disagree with the numerical simulation data from Degrez et al. [42] at the downstream of the separation region, which might be attributed to the numerical scheme employed. From Fig. 9, it also can be observed that the numerical solution of Vila-Pérez et al. [44] based on the DG approach, which was simulated in the condition of 3379 elements and P3, lies on top of the region of shock impingement. It is obvious that the current method with the entropy-based adaptive filtering technique is capable of accurately resolving the flow separation region at the shock impingement location.

The comparison of skin friction coefficient C_f on the plate is provided in Fig. 10. Again, Vila-Pérez et al. [44] fails to compute C_f in the shock impingement region accurately. Meanwhile, as mentioned above, C_f calculated in the current work also matches well with that of Mora et al. [43], but the numerical result from Degrez et al. [42] still shows clear deviation at the downstream of the separation region.
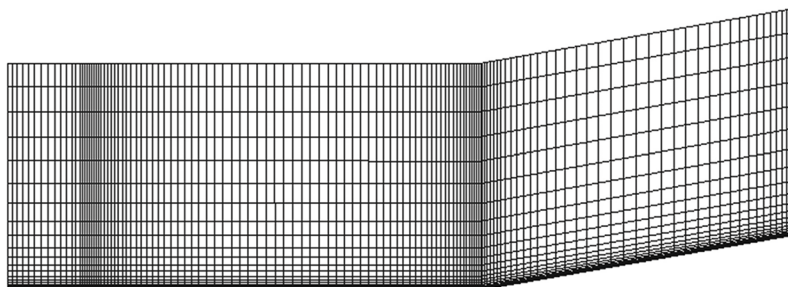
3.5 Supersonic compressible ramp flow

The flow separation caused by a ramp is a well-known phenomenon in the study of SWBLI. When the intensity of the shock waves generated by a ramp exceeds the capacity of the boundary layer to withstand them, the boundary layer separates at the corner. The ramp has a slope angle of 10°, with the freestream of $Ma = 3$ and $Re = 16,800$. The computational domain, as illustrated in Fig. 11, consists of 2921 grid points. In this scenario, the leading edge of the plate serves as the coordinate origin, and its distance to the corner represents the characteristic length. The left boundary corresponds to the inlet, positioned 0.2 away from the leading edge of the plate.
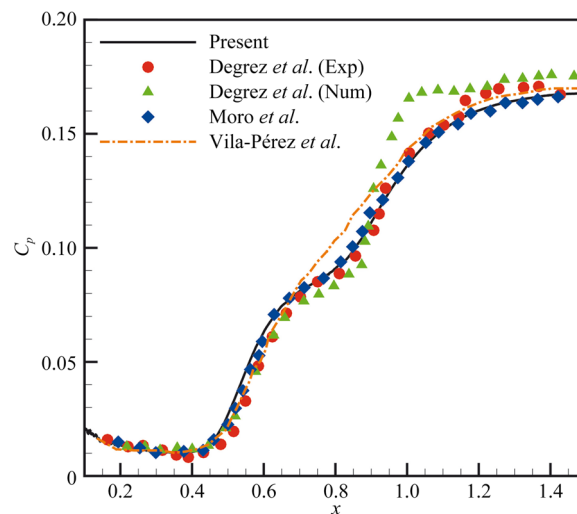
Fig. 9 Pressure coefficient on the plate for shock wave/boundary-layer interaction
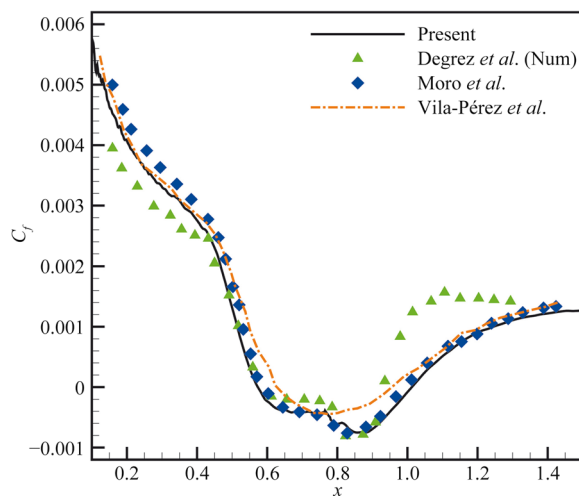
Fig. 10 Skin friction coefficient on the plate for shock wave/boundary-layer interaction
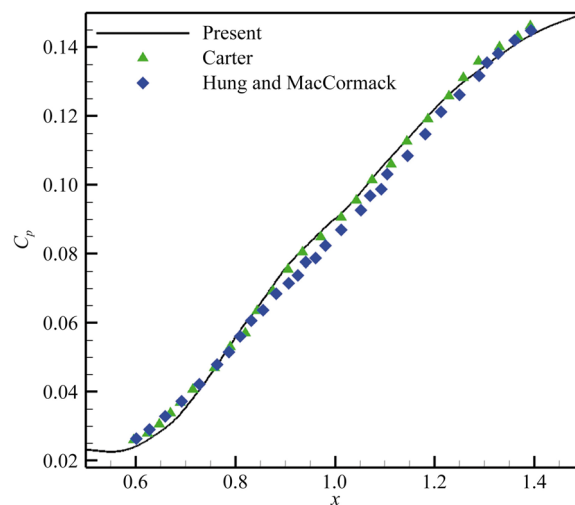

Fig. 11 Grid of supersonic compressible ramp flow

The top boundary represents the far-field boundary, situated at a distance of 0.575 from the plate. The right boundary represents the outlet, located at $x = 1.8$. The bottom surface, covering the range of $0 \leq x \leq 1.8$, is subjected to a no-slip boundary condition, with the temperature set as the total temperature of the incoming flow. The region of $-0.2 \leq x \leq 0$ is treated as a symmetry boundary.

Figure 12 displays the contours of density and Mach number, which clearly depicts the shock waves generated at the leading edge of the flat plate, as well as the compressible fan-shaped region induced by the ramp. Figure 13 illustrates the pressure coefficient C_p on the wall of the present study and the data in literature [45, 46]. It can be seen that the agreement between the current C_p and that in literature is found to be excellent. Figure 14 compares the present skin friction coefficient C_f with the reference data from Carter [45] with 2156 grid points and Hung and MacCormack [46] with 2408 elements, which are both second order accurate. It is evident that the current C_f agrees well with the data in literature. Meanwhile, Table 2 presents the positions of the separation point x_s and the reattachment point x_r on the ramp. The separation occurs when C_f changes from positive to negative, while the reattachment occurs when C_f changes from negative to positive. From the table, it can be observed that the locations of x_s and x_r in this study are consistent with those reported in literature [16, 45–48]. Therefore, the excellent agreement between the results in this study and the data in literature highlights the superior performance of FR-LBFS adopted.
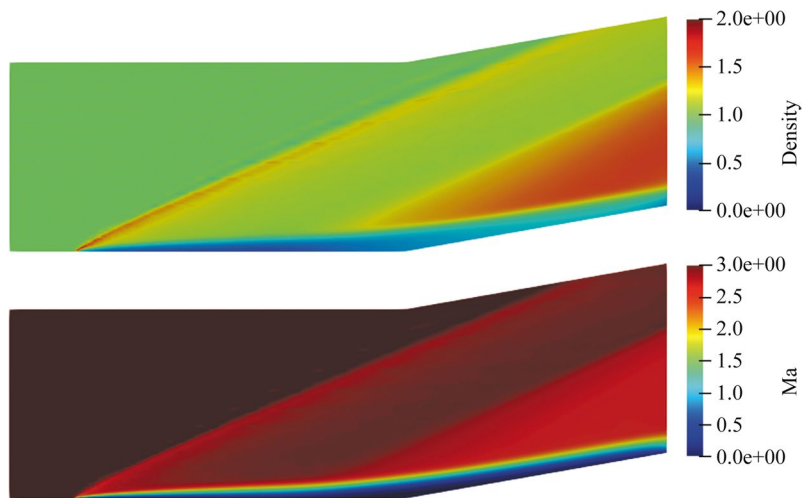
Fig. 12 Contours of density and Mach number for supersonic compressible ramp flow
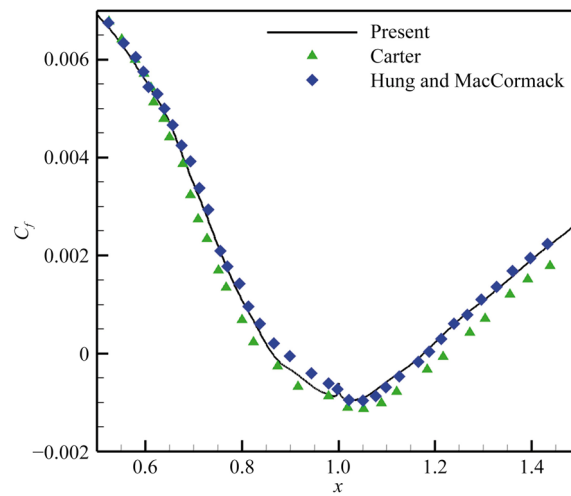

Fig. 13 Pressure coefficient on the wall for supersonic compressible ramp flow

3.6 Hypersonic flow over a leading edge ramp

Finally, a hypersonic flow over a leading edge ramp is simulated. The purpose is to gain insights into the unsteady behavior and heat transfer of shock-induced laminar boundary layer separation. The freestream is chosen as $Ma = 6$ and $Re = 8 \times 10^5$/m. Same as previous studies [9, 12, 13, 15], a 50 mm flat plate is attached to a $15°$ ramp. The wall temperature is set as $T_w = 300$ K. A well-structured grid, incorporating appropriate grid clustering, is generated as illustrated in Fig. 15.

To ascertain the grid independency, three different grids with sizes of 53×25, 107×51 and 151×75 are used. Figure 16(a) presents the comparison of pressure coefficient C_p between the result obtained in this study and those from Marini [9], John et al. [12] and Kane and Peetala [15], revealing a remarkable level of agreement. Figure 16(b) and (c)
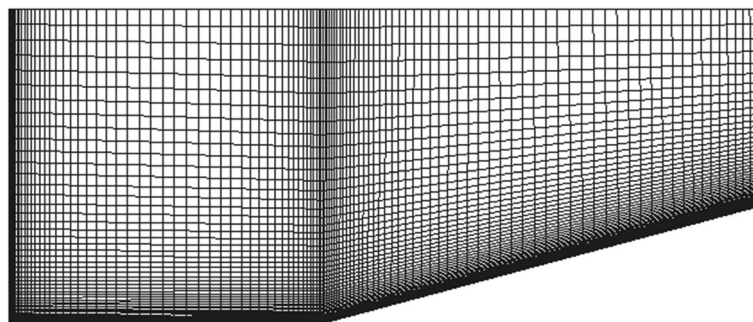
Fig. 14 Skin friction coefficient on the wall for supersonic compressible ramp flow

Table 2 Position of separation point x_s and reattachment point x_r on compressible ramp

	x_s	x_r
Present	0.86	1.18
Carter [45]	0.84	1.22
Hung and MacCormack [46]	0.89	1.18
Shakib et al. [47]	0.88	1.17
Mittal and Yadav [48]	0.89	1.13
Kotteda and Mittal [16]	0.88	1.17

Fig. 15 Grid of hypersonic flow over a leading edge ramp

respectively show the skin friction coefficient C_f and the Stanton number St of the current study and those of John et al. [12] with second order accuracy and 180×90 elements, demonstrating a high level of consistency and agreement.

From Fig. 16(a) and (b), it is found that when $1.5 < x < 2$, C_p and C_f with the grid of 53×25 display pronounced oscillations, whereas they exhibit comparable behavior with relatively consistent patterns at the grids of 107×51 and 151×75. Meanwhile, the grid of 107×51 is fine enough to produce accurate results. Moreover, compared
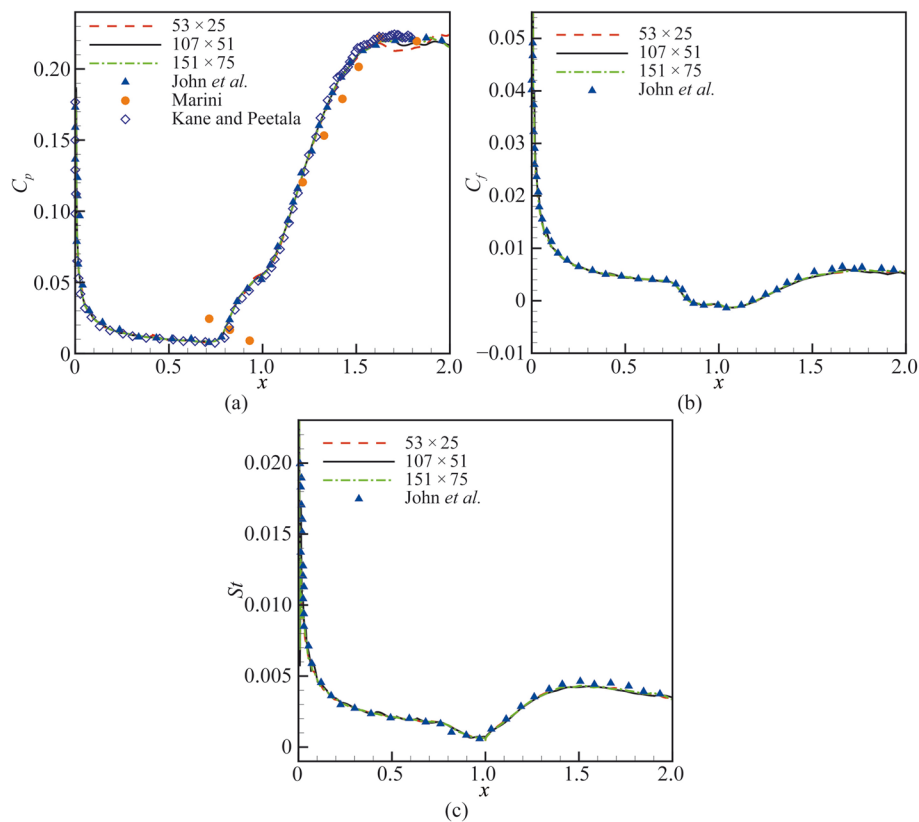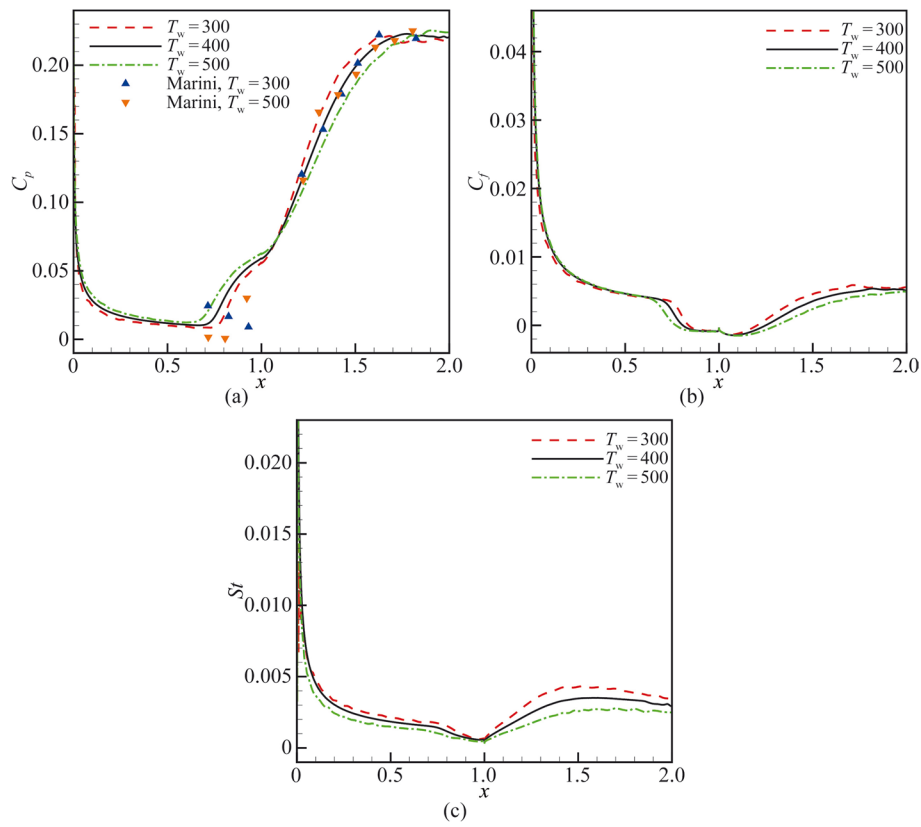
Fig. 16 (**a**) Pressure coefficient, (**b**) skin friction coefficient and (**c**) Stanton number over the wall with different grids for hypersonic flow over a leading edge ramp

with C_p from Kane and Peetala [15] using the grid of 420×240 with second order accuracy, the current method demonstrates improved stability in obtaining C_p while using a reduced grid resolution. This indicates that compared with low-order schemes, the present high order FR-LBFS has superior capability in simulating SWBLI.

Furthermore, to examine the capability of the present method in predicting heat transfer of SWBLI, two other wall temperatures of $T_w = 400\,K$ and $500\,K$ are considered. As seen in Fig. 17(a), C_p at $T_w = 300\,K$ and $500\,K$ shows excellent agreement with the experimental data from Marini [9]. With an increase in temperature, C_p ahead of the vortex ($x \approx 0.8$) shows a gradual increase, whereas C_p behind the vortex ($x \approx 1.2$) undergoes a gradual decrease. In Fig. 17(c), the decrease of St in the separation region can be observed, which is because the circulation of low temperature fluid appears in the same region. It is well known that C_f is a representation of the shear stress, which depends on the velocity gradient and viscosity. When the viscosity decreases with the decreasing temperature in the separation region, C_f also exhibits a decreasing trend. So C_f in Fig. 17(b) and St in Fig. 17(c) exhibit similar trends. Nevertheless, C_f and St exhibit a decline for the increased wall temperature case. That is because the increase in viscosity with the rising temperature results in an elevation of hydrodynamic and thickening of the thermal boundary layer. So the decrease in wall gradient leads to a reduction in C_f and St.

In addition, Table 3 displays the positions of the separation point x_s and the reattachment point x_r on the ramp. It can be observed that as the temperature increases, the length of the separation bubble (distance between x_r and x_s) also starts to increase from

Fig. 17 (**a**) Pressure coefficient, (**b**) skin friction coefficient and (**c**) Stanton number over the wall with different wall temperatures for hypersonic flow over a leading edge ramp

Table 3 Position of separation point x_s and reattachment point x_r on leading-edge compressible ramp

T_w	x_s	x_r
300 K	0.84	1.20
400 K	0.81	1.25
500 K	0.77	1.31

0.36 to 0.54. As discussed earlier, with increasing temperature, the thermal boundary layer becomes thicker, consequently leading to a higher susceptibility of separation.

4 Conclusions

This work investigates the utility of a high-order FR-LBFS with an entropy-based adaptive filtering method for predicting aerodynamics and heat transfer in viscous supersonic and hypersonic flows. The present approach is successfully employed to compute the double Mach reflection, viscous shock tube problem, shock wave/boundary layer interaction, supersonic compressible ramp flow and hypersonic flow over a leading edge ramp. These cases encompass complex shock interactions, flow separation, and small-scale structures, among others.

This study yielded several findings. Firstly, the current approach has demonstrated its capability to capture small scale structures in shock wave/boundary layer interaction. Secondly, in comparison to low order finite volume methods, the current approach achieves higher accuracy with fewer elements, and it exhibits minimal fluctuations in predicting aerodynamic coefficients. Finally, the numerical results of the present method are in good agreement with analytical or benchmark data, including aerodynamic coefficients and heat transfer. It demonstrates that the FR-LBFS employed has good performance in simulating SWBLI.

Availability of data and materials
The data that support the findings of this study are available from the corresponding author upon reasonable request.

Declarations

Competing interests
The authors declare that they have no competing interests.

References
1.　Gadd GE, Holder DW, Regan JD (1954) An experimental investigation of the interaction between shock waves and boundary layers. Proc R Soc A Math Phys Eng Sci 226(1165):227–253
2.　Hakkinen RJ, Greber I, Trilling L et al (1959) The interaction of an oblique shock wave with a laminar boundary layer. NASA Memo NASA-MEMO-2-18-59W
3.　Needham DA, Stollery JL (1966) Boundary layer separation in hypersonic flow. In: 3rd and 4th aerospace sciences meeting, New York, 24-26 January 1966
4.　Elena M, Lacharme JP (1988) Experimental study of a supersonic turbulent boundary layer using a laser Doppler anemometer. J Mec Theor Appl 7:175–190
5.　Settles GS, Fitzpatrick TJ, Bogdonoff SM (1979) Detailed study of attached and separated compression corner flowfields in high Reynolds number supersonic flow. AIAA J 17:579–585
6.　Settles GS, Dodson LJ (1991) Hypersonic shock/boundary-layer interaction database. In: 22nd fluid dynamics, plasma dynamics and lasers conference, Honolulu, 24-26 June 1991
7.　Settles GS, Dodson LJ (1994) Hypersonic shock/boundary-layer interaction database: new and corrected data. NASA Contr Rep NASA-CR-177638
8.　Bookey P, Wyckham C, Smits A et al (2005) New experimental data of STBLI at DNS/LES accessible Reynolds numbers. In: 43rd AIAA aerospace sciences meeting and exhibit, Reno, 10-13 January 2005
9.　Marini M (1998) Effects of flow and geometry parameters on shock-wave boundary-layer interaction phenomena. In: 8th AIAA international space planes and hypersonic systems and technologies conference, Norfolk, 27-30 April 1998
10.　Hankey WL Jr, Holden MS (1975) Two-dimensional shock wave-boundary layer interactions in high speed flows. AGARD Rep AG-203-0134
11.　Rizzetta DP, Mach KD (1989) Comparative numerical study of hypersonic compression ramp flows. In: 20th fluid dynamics, plasma dynamics and lasers conference, Buffalo, 12-14 June 1989
12.　John B, Kulkarni VN, Natarajan G (2014) Shock wave boundary layer interactions in hypersonic flows. Int J Heat Mass Transf 70:81–90
13.　John B, Kulkarni V (2014) Numerical assessment of correlations for shock wave boundary layer interaction. Comput Fluids 90:42–50
14.　Brioso DE, Gai SL, Neely AJ (2020) Wall temperature effects on two-dimensional hypersonic laminar separation. In: AIAA scitech 2020 forum, Orlando, 6-10 January 2020
15.　Kane AA, Peetala RK (2020) Numerical investigation of the transient nature of a laminar separation bubble in hypersonic flow. Fluid Dyn 55:511–524

16. Kotteda VMK, Mittal S (2014) Stabilized finite-element computation of compressible flow with linear and quadratic interpolation functions. Int J Numer Methods Fluids 75:273–294
17. Moro D, Nguyen NC, Peraire J (2016) Dilation-based shock capturing for high-order methods. Int J Numer Methods Fluids 82:398–416
18. Adams NA (1998) Direct numerical simulation of turbulent compression ramp flow. Theor Comput Fluid Dyn 12:109–129
19. Adams NA (2000) Direct simulation of the turbulent boundary layer along a compression ramp at $M = 3$ and $Re_\theta =$ 1685. J Fluid Mech 420:47–83
20. Wu M, Martin MP (2007) Direct numerical simulation of supersonic turbulent boundary layer over a compression ramp. AIAA J 45:879–889
21. Loginov MS, Adams NA, Zheltovodov AA (2006) Large-eddy simulation of shock-wave/turbulent-boundary-layer interaction. J Fluid Mech 565:133–169
22. Katzer E (1989) On the lengthscales of laminar shock/boundary-layer interaction. J Fluid Mech 206:477–496
23. Harten A, Engquist B, Osher S et al (1987) Uniformly high order accurate essentially non-oscillatory schemes, III. J Comput Phys 71:231–303
24. Hu C, Shu CW (1999) Weighted essentially non-oscillatory schemes on triangular meshes. J Comput Phys 150:97–127
25. Reed WH, Hill TR (1973) Triangular mesh methods for the neutron transport equation. Los Alamos Scientific Lab Rep LA-UR-73-479
26. Kopriva DA, Kolias JH (1996) A conservative staggered-grid Chebyshev multidomain method for compressible flows. J Comput Phys 125:244–261
27. Huynh HT (2007) A flux reconstruction approach to high-order schemes including discontinuous Galerkin methods. In: 18th AIAA computational fluid dynamics conference, Miami, 25-28 June 2007
28. Hesthaven JS, Warburton T (2008) Nodal discontinuous Galerkin methods: algorithms, analysis, and applications. Springer, New York
29. Yang LM, Shu C, Wu J (2016) A hybrid lattice Boltzmann flux solver for simulation of viscous compressible flows. Adv Appl Math Mech 8:887–910
30. Dzanic T, Witherden FD (2022) Positivity-preserving entropy-based adaptive filtering for discontinuous spectral element methods. J Comput Phys 468:111501
31. Vincent PE, Castonguay P, Jameson A (2011) A new class of high-order energy stable flux reconstruction schemes. J Sci Comput 47:50–72
32. Persson PO, Peraire J (2009) Curved mesh generation and mesh refinement using Lagrangian solid mechanics. In: 47th AIAA aerospace sciences meeting including the new horizons forum and aerospace exposition, Orlando, 5-8 January 2009
33. Yu M, Wang ZJ, Liu Y (2014) On the accuracy and efficiency of discontinuous Galerkin, spectral difference and correction procedure via reconstruction methods. J Comput Phys 259:70–95
34. Zhang C, Li QB, Fu S et al (2018) A third-order gas-kinetic CPR method for the Euler and Navier–Stokes equations on triangular meshes. J Comput Phys 363:329–353
35. Roe PL (1981) Approximate Riemann solvers, parameter vectors, and difference schemes. J Comput Phys 43:357–372
36. Liou MS, Steffen CJ Jr (1993) A new flux splitting scheme. J Comput Phys 107:23–39
37. Gottlieb S, Shu CW, Tadmor E (2001) Strong stability-preserving high-order time discretization methods. SIAM Rev 43:89–112
38. Cockburn B, Shu CW (1998) The local discontinuous Galerkin method for time-dependent convection-diffusion systems. SIAM J Numer Anal 35:2440–2463
39. Witherden FD, Farrington AM, Vincent PE (2014) PyFR: an open source framework for solving advection-diffusion type problems on streaming architectures using the flux reconstruction approach. Comput Phys Commun 185:3028–3040
40. Laskowski W, Rueda-Ramírez AM, Rubio G et al (2020) Advantages of static condensation in implicit compressible Navier–Stokes DGSEM solvers. Comput Fluids 209:104646
41. Daru V, Tenaud C (2000) Evaluation of TVD high resolution schemes for unsteady viscous shocked flows. Comput Fluids 30:89–113
42. Degrez G, Boccadoro CH, Wendt JF (1987) The interaction of an oblique shock wave with a laminar boundary layer revisited. An experimental and numerical study. J Fluid Mech 177:247–263
43. Moro D, Nguyen NC, Peraire J et al (2017) Mesh topology preserving boundary-layer adaptivity method for steady viscous flows. AIAA J 55:1970–1985
44. Vila-Pérez J, Giacomini M, Sevilla R et al (2021) Hybridisable discontinuous Galerkin formulation of compressible flows. Arch Comput Methods Eng 28:753–784
45. Carter JE (1972) Numerical solutions of the Navier-Stokes equations for the supersonic laminar flow over a two-dimensional compression corner. NASA Tech Rep NASA-TR-R-385
46. Hung CM, MacCormack RW (1976) Numerical solutions of supersonic and hypersonic laminar compression corner flows. AIAA J 14:475–481
47. Shakib F, Hughes TJR, Johan Z (1991) A new finite element formulation for computational fluid dynamics: X. The compressible Euler and Navier-Stokes equations. Comput Methods Appl Mech Eng 89:141–219
48. Mittal S, Yadav S (2001) Computation of flows in supersonic wind-tunnels. Comput Methods Appl Mech Eng 191:611–634

Publisher's Note